MISSIONE 4
ISTRUZIONE RICERCA

D4.15.2: Report on the optimization of morphological image processing approach algorithm for ABLH determination [B10]

Finanziato dall'Unione europea NextGenerationEU
Ministero dell'Università e della Ricerca
Italiadomani PIANO NAZIONALE DI RIPRESA E RESILIENZA

Deliverable number:	D4.15.2
Work package:	WP4 – Atmosphere
Intermediate Objective:	IO4.5
Deliverable type:	X Document, report
	☐ Websites, patent filings, videos, etc.
	☐ Other: please specify .....
Dissemination level:	X Public
	☐ Restricted
Estimated delivery (bimester):	B10
Actual delivery date:	30-06-2024
Author(s) (Partner-OU):	Giuseppe D'Amico, Aldo Amodeo, Davide Amodio, Francesco Cardellicchio, Benedetto De Rosa, Nicola Gianluca Di Fiore, Ilaria Gandolfi, Aldo Giunta, Emilio Lapenna, Teresa Laurita, Fabrizio Marra, Michail Mytilinaios, Lucia Mona, Nikolaos Papagiannopoulos, Serena Trippetta, Marco Rosoldi, Donato Summa, Gemine Vivone, Canio Colangelo (CNR-IMAA)
Reviewed by:	Francesco Cairo (CNR-ISAC)
Note:	

IR0000032 – ITINERIS, Italian Integrated Environmental Research Infrastructures System - CUP B53C22002150006 (D.D. n. 130/2022)
Funded by EU - Next Generation EU
Mission 4 “Education and Research” - Component 2: “From research to business” -
Investment 3.1: “Fund for the realisation of an integrated system of research and innovation infrastructures”

Table of contents

List of figures

List of tables

1. INTRODUCTION

This deliverable provides a report on the assessment and optimization of MIPA (Morphological Image Processing Approach) algorithm[1] for the retrieval of Atmospheric Boundary Layer Height (ABLH) from High Power Lidar (HPL) data. MIPA has been developed at CNR-IMAA in the framework of ACTRIS and it has been already tested on several HPL datasets showing, in general, quite good performance with respect to the traditional ABLH retrieval techniques. The main MIPA novelty consists in operating on timeseries of lidar profiles and not on single lidar profile (as most of lidar-based ABLH retrievals available in literature do). Consequently, the ABLHs retrieved by MIPA consider not only the vertical dynamic of single lidar profiles, but also the correlation among contiguous (in time) lidar observations. Moreover, as MIPA works mainly on vertical and time correlations of the input dataset, the results do not rely on absolute intensities but on the corresponding relative variations. This feature makes MIPA a robust algorithm and opens the possibility to extend its applicability to a large number of lidar systems with different characteristics in terms of Signal to Noise Ratio (SNR), detection and acquisition type.

As it will be described later, to deliver accurate results, MIPA first needs to be tuned by setting a few configurational parameters appropriately. The optimization of MIPA configurational parameters can be done by using specific input dataset(s) for which accurate references in terms of ABLH are known. Optimal MIPA parameters are the ones for which the delivered ABLHs are closest to the reference ones. In the following, we refer to such procedure as MIPA *optimization/validation*. Once this initial optimization phase is completed (considering the algorithm characteristics already mentioned), MIPA is expected to deliver accurate results also when applied (with the same configuration) on observations made by different lidar systems.

Consequently, MIPA can be evaluated also on ceilometer (Low Power Lidar - LPL) observations which are typically available 24/7 with lower overlap with respect to HPLs but with poorer SNR. This deliverable will cover MIPA *optimization/validation* made considering HPL datasets only. The evaluation of the optimized MIPA configuration on ceilometer observations will be the main topic of the deliverable D4.15.3 due by B15.

To make MIPA optimization/validation possible, a dedicated measurement campaign has been performed at CIAO (CNR-IMAA Atmospheric Observatory) in Spring 2024. During this campaign a quite complete set of atmospheric sensors has been operative continuously, including HPLs, LPLs, Doppler lidar, Radar systems, as well as both manual and automatic radiosounding systems. Further details about the characteristics of all the instruments involved in the campaign can be found in deliverable D.4.15.1. Here we will focus on a short description of the observations/datasets we have selected for MIPA *optimization/validation* and the approach we used for the validation.

2. MEASUREMENT CAMPAIGN

The CIAO ABLH measurement campaign took place at CNR-IMAA (40.60N, 15.72E, 760 m a.s.l.) from 15 April 2024 up to 1 May 2024. The main goal is to have different types of remote sensing instruments operating simultaneously and continuously 24/7 together with frequent radiosondes'

[1] *Vivone, G., D'Amico, G., Summa, D., Lolli, S., Amodeo, A., Bortoli, D., and Pappalardo, G.*: **Atmospheric boundary layer height estimation from aerosol lidar: a new approach based on morphological image processing techniques**, Atmos. Chem. Phys., 21, 4249–4265, https://doi.org/10.5194/acp-21-4249-2021, 2021

launches to establish a reference dataset for the ABLH retrieval. As different ABLH retrievals are based on different assumptions, the quite large number of instruments participating in the campaign is expected to be an added value to assess the impact of these assumptions under different atmospheric conditions. ABLH retrievals from lidar measurements, for example, use the atmospheric aerosols as tracers of the ABL, which is supposed to be always well-mixed. This assumption may show some limitations when the aerosol content is particularly low or in case of low clouds and/or precipitation (when lidar measurements are not possible). Moreover, particularly low ABLHs (below the lidar full overlap height) are not detectable, independently of the retrieval algorithm. In addition, there are different conditions under which the ABL is formed (non-turbulent, cloud-driven, convective, wind shear, etc.) and, consequently, ABL retrieval from the lidar measurements should be evaluated in each one of those. In this context, the use of sensors like Doppler lidar and radar can help in detecting the lidar limitations and can provide a useful ABL classification to be correlated with ABLH retrieval results.

Concerning the remote sensing instrumentations, two Doppler radars (MIRA35 and MIRA35C by METEK), a Doppler lidar (Stream Line^{XR} by Halo Photonics), three ceilometers (CL31 and CL51 by VAISALA, CHM15k by Lufft) and a microwave radiometer (RPG-HATPRO-G5 by Radiometer Physics) were operating continuously for the whole campaign period. Moreover, a fixed multi-wavelength Raman lidar POLPO (POtenza Lidar for Particle Observation) and a mobile and more compact multi-wavelength Raman lidar MEDUSA both by Raymetrics were operating continuously whenever the atmospheric conditions were suitable for lidar observations (no rain precipitation/low clouds).

During the campaign many radiosoundings have been performed, with very high launch frequency, (up to 8 launches per day), during selected days considered particularly interesting for the campaign purposes. Such a high launch frequency is a crucial factor for the assessment of MIPA algorithm, as the ABLH values calculated out of radiosounding observations provide an appropriate reference against which compare the ABLHs retrieved by MIPA. CIAO is the ideal site for performing this kind of experiment, as it is equipped with two radiosounding systems (one of which with an automatic launcher and both by VAISALA) which are part of GCOS Reference Upper Air Network (GRUAN). The exact scheduling of the radiosondes' launches has been evaluated case by case based on high-resolution weather model forecasts, with denser launches typically performed in correspondence of ABL transition periods or during special events like dust intrusions.

Additionally, a quite complete set of in-situ instrumentations was operating continuously for the whole campaign period providing useful information for the aerosol full characterization at the ground. In particular, data from aethalometer (AE33 by Aerosol Magee Scientific), nephelometer (Aurora 3000 by Acoem), aerodynamic particle sizer (APS 3321 by TSI Incorporated), condensation particle counter (CPC 3750 by TSI Incorporated), scanning mobility particle sizer (SMPS 3938 by TSI) and PMx samplers are available.

We underline here that the final goal of this measurement campaign is to provide all ACTRIS Italian stations operating an active aerosol remote sensing component (considering both HPL and LPL measurements) with a well assessed, unattended and automatic tool (MIPA) for the retrieval of the ABLH. The achievement of this objective will allow ITINERIS to deliver homogenized ABLHs in near real time for all ACTRIS Italian stations, coherent with the 100% digital outcome of the project.

Moreover, the dataset collecting all the measurements performed during the campaign will be a valid testbed for the development of new algorithms to retrieve the ABLH like for example the ones based on machine learning approaches.

3. CASE STUDIES

As the primary goal of this deliverable is MIPA *optimization/validation,* we describe here not all the observations made during the whole campaign but only specific case studies. The case studies have been selected trying to meet as much as possible all the conditions ensuring an optimal input dataset for MIPA. In this way we expect to archive an accurate optimization of all MIPA configuration parameters that, in a second step, can be used to operate MIPA also under not optimal conditions. The optimal input dataset to evaluate MIPA performance is composed by a timeseries of vertical profiles of any variable proportional to the concentration of the considered ABL tracers (e.g. aerosols or other atmospheric constituents like water vapor) meeting the following conditions:

A) continuous and long as much as possible (ideally with no gaps or with rare and small gaps)

B) high vertical and time resolution

C) high/moderate SNR

Modern HPLs can easily provide a dataset with all these characteristics as they can deliver continuous timeseries of total attenuated backscatter (or even range corrected signal) with time resolution lower than 1 minute, vertical resolution of few meters, relatively high SNR and at different wavelengths. Considering that in the total elastically backscattered lidar signal the longer is the wavelength the higher is the contrast of the contribution due to the particles with respect to one due to the molecules, to guarantee an accurate ABLH determination it is convenient to consider the longer wavelength available (which in general is at 1064nm).

It could be possible that in lidar observations there are gaps which typically occur in correspondence of rain precipitations (when lidar observations are not possible or very challenging) or while the lidar is performing internal calibration measurements (like for example dark measurements or depolarization calibration cycles). In the latter case the gaps are usually minimal (typically 10-20 minutes every 12-24h) and from practically point of view have no important effects on MIPA retrieval.

According to that we selected two case studies which represent the longest and almost continuous HPL observations available during the whole campaign:

- **Case study 1:** from 2024-04-28 03:00 UTC up to 2024-05-01 00:00UT
- **Case study 2:** from 2024-04-15 00:00 UTC up to 2024-04-16 12:00UT

We intensified the radiosoundings scheduling during these case studies to assure the establishment of a representative ABLH reference dataset. Further details about the launches performed and the calculation of the reference ABLH values are provided in section 5.

It was not possible to select longer and continuous HPL datasets mainly because of persistent or intermitted rain precipitations occurred over the measurement site.

3.1 Case study 1

This case study includes 69 hours of almost continuous HPL observations made by POLPO. It starts at 2024-04-28 03:00 UTC and ends at 2024-05-01 00:00 UTC because of incoming low rain clouds. Fig. 1 shows the timeseries of total attenuated backscatter (on the left column) and the volume linear depolarization ratio (on the right column) at 3 different wavelengths (1064, 532 and 355nm) as delivered by the Single Calculus Chain (SCC), the standard and quality assured tool for the automatic processing of raw data of ACTRIS aerosol remote sensing observations.

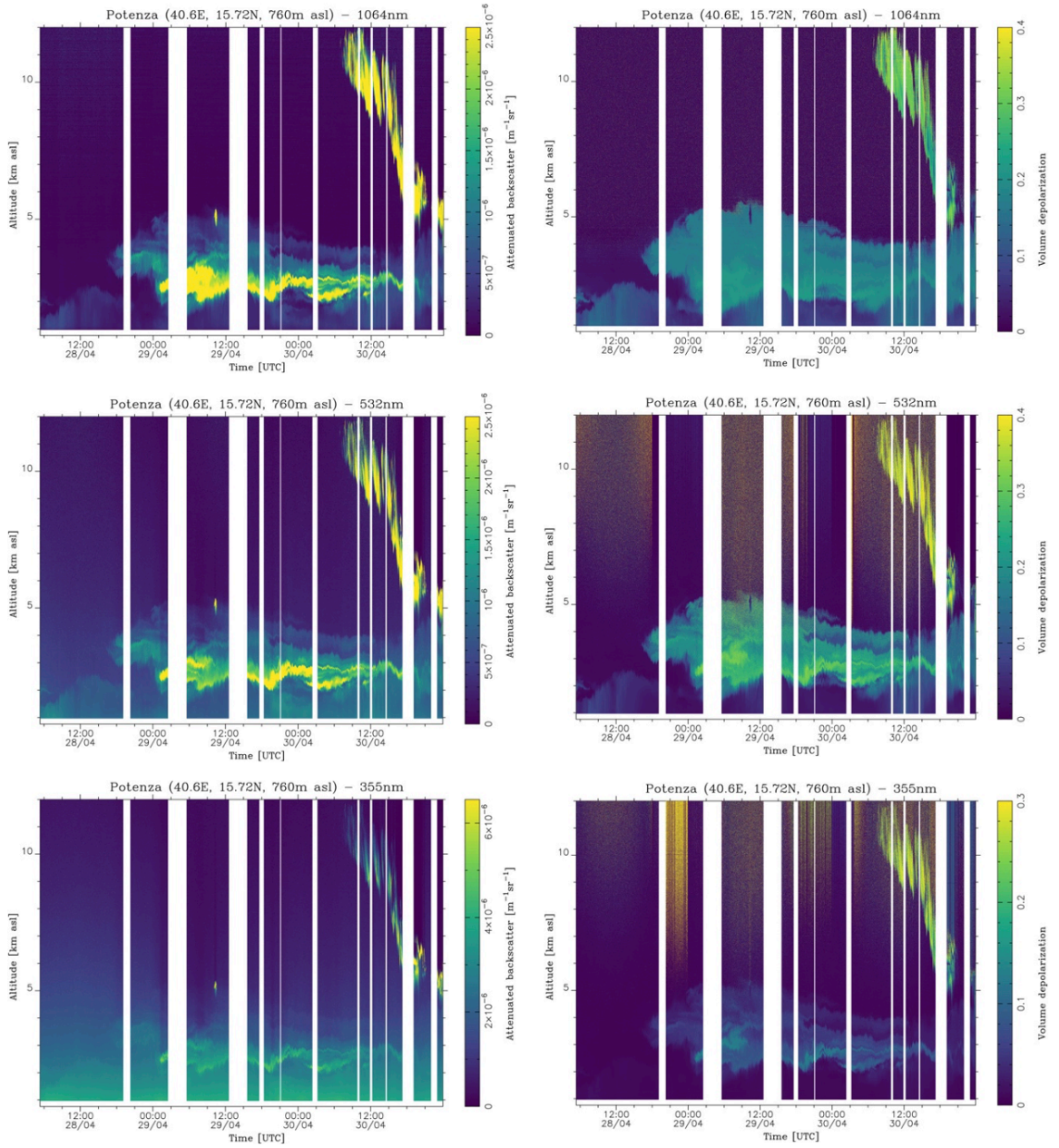

Figure 1: Case study 1: total attenuated backscatter (on the left) and volume linear depolarization (on the right) at 1064 (top row), 532 (middle row) and 1064nm (bottom row) measured by CIAO lidar POLPO.

All the measurement gaps (white strips in the figure) are due to internal calibration cycles (mainly dark measurements), switch from daytime to nighttime lidar configuration (or the other way around), and small instrumental issues.

This case study is quite interesting from many points of view.

On 28 April, the typical diurnal evolution of the ABL is clearly visible: due to the sunrise the ABLH starts to increase in the morning, and it reaches a maximum of about 2.5 km asl at around 15:00 UTC

when the solar convective action is maximum. Later, as expected, the ABLH starts to decrease assuming values below the lidar full overlap height (which is about 250-300m) after the sunset.

On 29 April, a similar behavior is observed, but at same time a quite intense dust layer is visible in the region above ABL between 2 and 5 km asl. However, the effect of this layer on the ABL dynamics is minimal as its evolution looks quite similar to the one observed in the previous day.

The situation changes drastically on 30 April when the compressive effect of the dust layer becomes stronger affecting the normal evolution of the ABL[2,3]. The formation of gravity waves clearly visible in the maps within the dust layer is a clear indication of two opposite tendencies: convective pushing up due to solar activity and pulling down due to the dust layer gravity deposition. Moreover, while on 29 April the dust layer keeps on staying above the ABL without intruding (or intruding minimally) in it, on 30 April it starts to penetrate much more within the ABL and later to deposit on the ground. This reconstruction is confirmed also by the in-situ observations reported in Fig. 2.

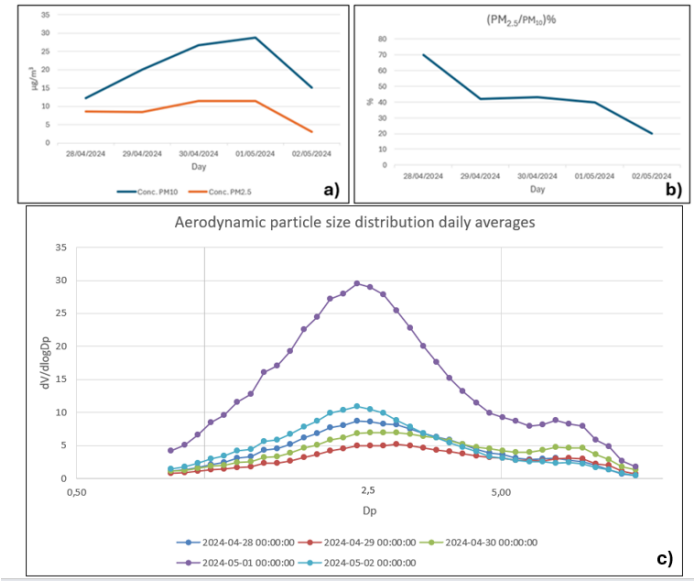

Figure 2: In situ measurements performed at CIAO from 28 April to 2 May 2024. a) Evolution of PM10 and PM2.5 concentrations b) Evolution of the percentage ratio (PM2.5/PM10) c) Aerodynamic particle size distribution daily averages from 28-04-2024 to 02-05-2024.

In the period under examination the particulate at ground was sampled on Teflon filters (Pall Life Science Teflon, W/RING 2 um 47 mm) using a SWAM 5a Dual Channel Monitor PMx sampler; this instrument was used for the simultaneous sampling on two independent lines (PM_{10} and $PM_{2.5}$) with associated mass measurement.

In Fig. 2 (a) we report the temporal pattern of PM_{10} and $PM_{2.5}$ concentrations from 28 April to 2 May showing a slow and continuous increase in PM_{10} values until reaching the maximum value on 1 May (28.7 µg/m^3). From Fig. 2 (b) we can observe, in detail, the evolution of the percentage ratio

[2] *C. Flamant, J.-P. Chaboureau, D. J. Parker, C. M. Taylor, J.-P. Cammas, O. Bock, F. Timouk, J. Pelon*, **Airborne observations of the impact of a convective system on the planetary boundary layer thermodynamics and aerosol distribution in the inter-tropical discontinuity region of the West African Monsoon**, Q.J.R. Meteorol. Soc., 133: 1175-1189. https://doi.org/10.1002/qj.97

[3] *H. Choi, Y.H. Zhang, K.H. Kim*, **Sudden high concentration of TSP affected by atmospheric boundary layer in Seoul metropolitan area during duststorm period**, Environment International, Volume 34, Issue 5, https://doi.org/10.1016/j.envint.2007.12.023.

($PM_{2.5}/PM_{10}$) for the period of interest. The observed trend corresponds to a decrease in the percentage ratio (69.9% to 19.9%) and, therefore, to an increase in the size of the particles falling to the ground in the days following 28 April.

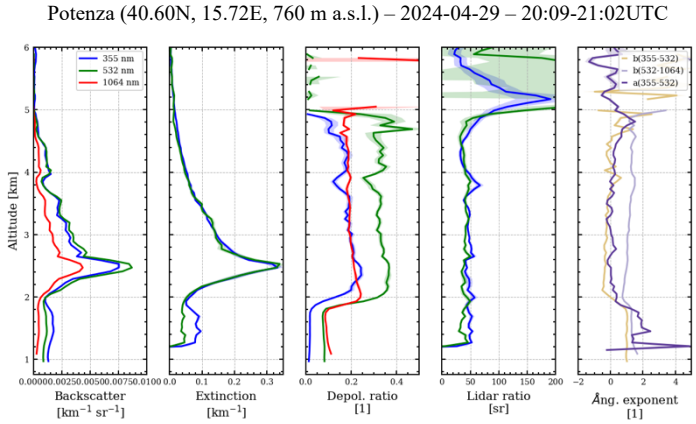

Figure 3: Case study 1: Optical characterization of the dust layer between 2 and 5 km observed on 29 April by POLPO lidar. From left to the right: aerosol backscatter at 355, 532, 1064nm, aerosol extinction at 355 and 532nm, particle linear depolarization ratio at 355, 532, 1064nm, lidar ratios at 355 and 532 and Angström exponent. All the vertical profiles have been obtained by averaging lidar signals between 20:09 and 21:02 UTC.

This trend is confirmed by the online observations at ground level, by the APS spectrometer that provides high-resolution real-time aerodynamic measurements for the coarse fraction of the particle in the size range from 0.8 to 10 µm and so plays a key role in dust studies. Fig. 2 (c) shows the aerodynamic particle size distribution daily averages obtained by APS from 28 April to 2 May and provides complementary information to that obtained through the PMx sampler. Indeed, Fig. 2 (c) distinctly illustrates that there is a noticeable increase in the concentration of particles on 1 May compared to the previous and subsequent days.

The in-situ observations confirm the previously advanced hypotheses obtained through lidar measurements by demonstrating that when the dust layer penetrates much further into the ABL there is a greater return of coarse particles to the ground level. Anyway, the importance of the chemical analysis on filters will be crucial to understand the nature of the PM and for retrieving the sources.

The dust nature of the observed layer is supported by the vertical profiles reported in Fig. 3 showing (from left to the right) aerosol backscatter at 355, 532, 1064nm, aerosol extinction at 355 and 532nm, particle linear depolarization ratio at 355, 532, 1064nm, lidar ratios and Angström exponent, as measured by POLPO. All the profiles have been obtained by averaging lidar measurements between 20:09 and 21:02 UTC on 29 April. The measured values of depolarization ratio, lidar ratio and Angström exponent within the layer extending from 2 up to 5km are the typical ones corresponding to dust particles.

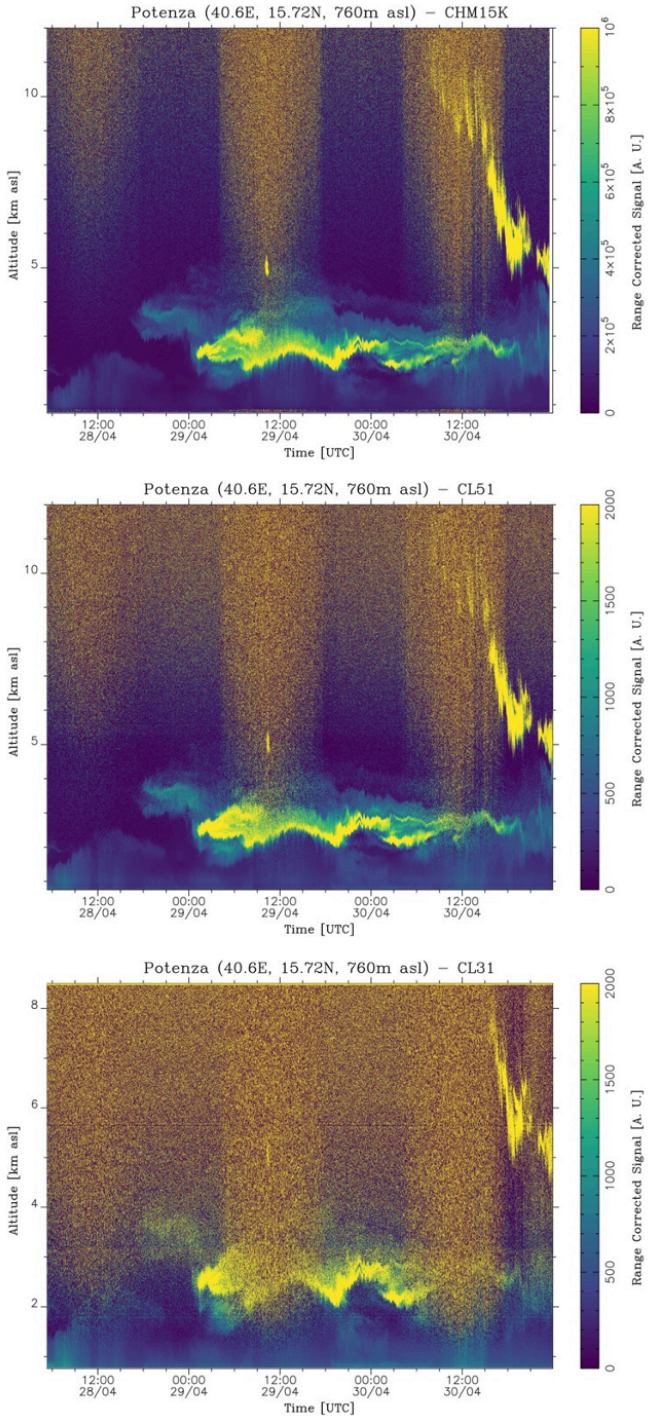

Figure 4: Case study 1: timeseries of range corrected signal measured by CHM15k (top), CL51 (middle) and CL31 (bottom) ceilometers.

It is interesting to mention that the values of lidar ratio and Angström exponents measured for the same layer on 28 April (not shown) are slightly larger than the ones reported in Fig. 3. This seems to support particle size slightly larger (and probably heavier) on 29 April with respect to 28 April explaining why dust start to intrude in the ABL more efficiently on 29-30 April. Such variation of

the dust layer properties can be due to a gradually reducing level of mixing with other smaller and lighter particles.

For completeness we report in Fig. 4 the timeseries of range corrected signal measured by CHM15k ceilometer (top), CL51 (middle), CL31 (bottom) in correspondence of this case study. By comparing Figs. 1 and 4 advantages and disadvantages of HPL with respect to LPL observations are evident: SNR is much better for HPL while overlap and observation continuity is usually better for LPL.

3.2 Case study 2

This case study includes 36 hours of almost continuous HPL observations made by POLPO. It starts at 2024-04-15 00:00 UTC and ends at 2024-04-16 12:00 UTC. Fig. 5 shows the same quantities reported in Fig. 1 but for the second case study.

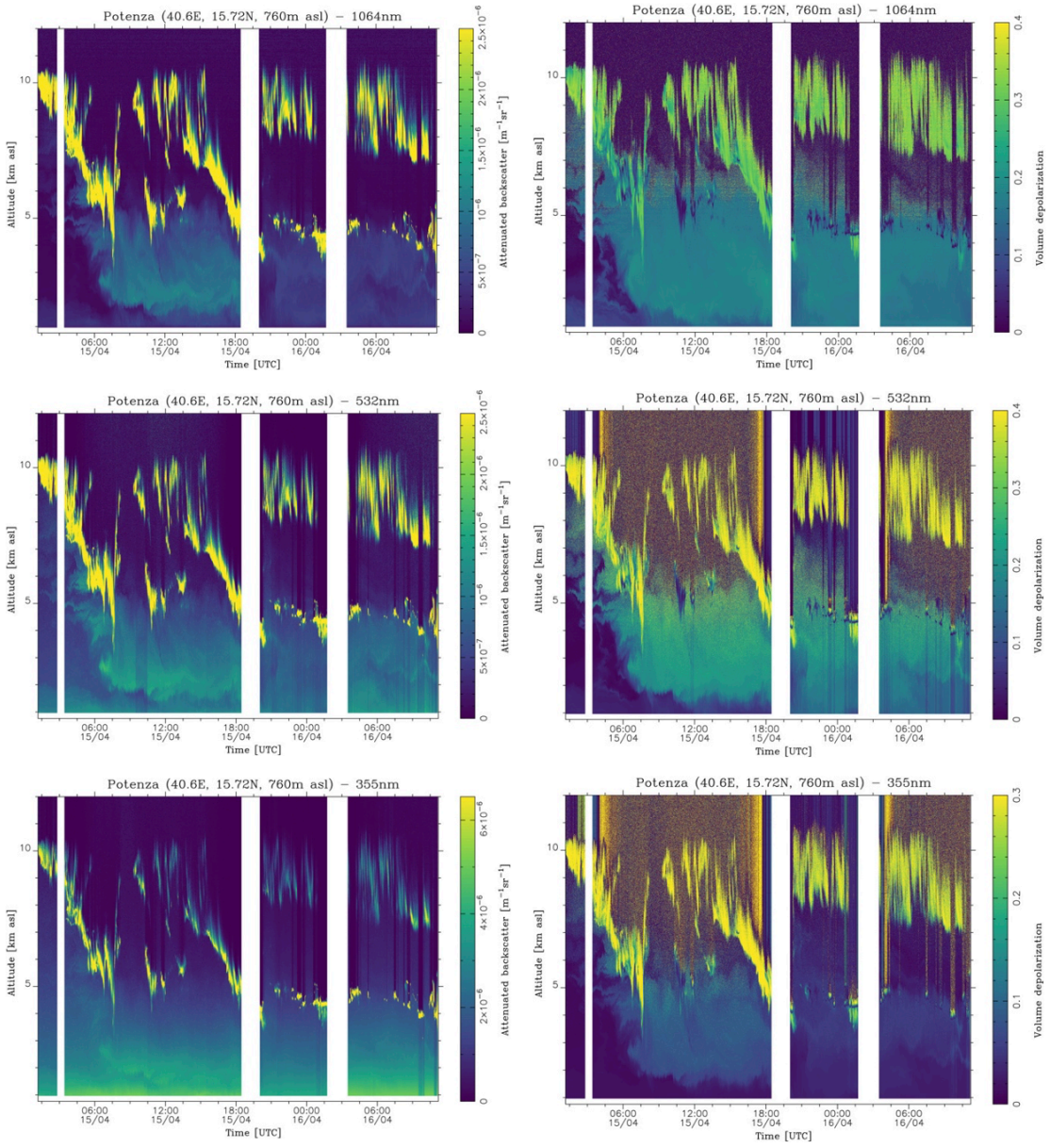

Figure 5: Case study 2: total attenuated backscatter (on the left) and volume linear depolarization (on the right) at 1064 (top row), 532 (middle row) and 1064nm (bottom row) measured by CIAO lidar POLPO.

On 15 April, the plot shows a dust layer extending very close to the ground. This layer has a compressive effect on the ABL dynamics similar to the one described for the layer observed on 30 April but much stronger. This can be due to different particle dimension of the layer above the ABL in the two case (compare Fig. 3 and 7) and/or to less convective ABL regime due to lower temperature on the ground measured on 15 April with respect to 30 April. In this case the presence of the layer does not allow the ABL to make the typical diurnal growth and, consequently, it remains confined at heights below 1.5km asl. Additionally, the dust layer intrudes the ABL and reaches the ground right after 12:00 UTC (this is particularly clear by looking at depolarization ratio maps). It's worth noting that during that day, this dust layer was clearly visible on the measurement site, reducing the visibility consistently. During the next day (16 April) the dust layer is still present, but its concentration is reduced allowing the ABLH to growth more than on the previous day. In-situ measurements reported in Fig. 6 support this hypothesis.

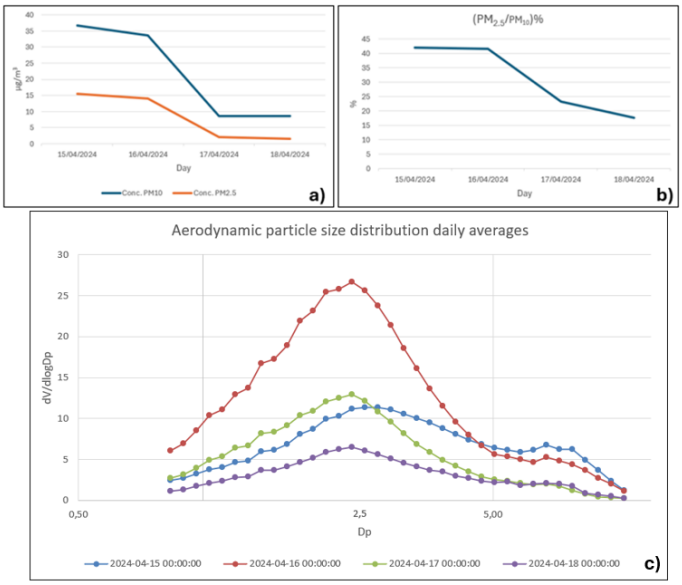

Figure 6: In situ measurements performed at CIAO from 15-18 April 2024 a) Evolution of PM10 and PM2.5 concentrations b) Evolution of the percentage ratio (PM2.5/PM10) c) Aerodynamic particle size distribution daily averages.

In Fig. 6 (a) we report the temporal pattern of PM_{10} and $PM_{2.5}$ concentrations from 15 April to 18 April while in Fig. 6 (b) we report the percentage ratio ($PM_{2.5}/PM_{10}$) for the same period. In Fig 6 (a) we observe a higher concentration of PM on 15 April (PM_{10}: 36.7 µg/m^3, $PM_{2.5}$: 15.4 µg/m^3) and on 16 April (PM_{10}: 33.6 µg/m^3, $PM_{2.5}$: 14 µg/m^3) with respect to the following days when the concentration of PM decreases significantly; instead, in Fig. 6 (b) it is interesting to note that the percentage ratio tends to decrease (from 42.0% on 15 April to 17.6% on 18 April). This result indicates that on 15 and 16 April there was a notable increase in both fine (<2.5 µm) and coarse (from 2.5 to 10 µm) particles concentration. In the following days, even if the PM concentration decreases considerably, the contribution of coarse particles is greater than fine particles probably meaning that there is still a contribution of dust from the higher levels of the atmosphere. This trend is confirmed by the daily averages of the aerodynamic particle size distribution obtained by APS from 15 to 18 April reported in Fig. 6 (c). Fig. 6 (c) clearly illustrates that on 15 and especially on 16 April there was a notable increase in both fine and coarse particles concentration with respect to what happens during the following days.

However, we will be able to study the nature of the particulate and compare the two case studies when we will have the chemical analyses. The filters collected during the campaign will be sent to LABEC laboratory of INFN in Florence which will make elemental composition and concentration of all samplers using the Particle-induced X-ray emission (PIXE). Additionally, the filters will also

undergo further analyses, such as with a scanning electron microscope (SEM), which will be used to examine the morphology of the particles, including information on shape, size, and structure.

Furthermore, we report the intensive and extensive optical properties of the observed layer as measured by POLPO (Fig. 7) in daytime configuration (no Raman channels available) and the range corrected signal timeseries measured by the ceilometers (Fig. 8). As before, the lidar observations support the presence of dust particles within the observed layer.

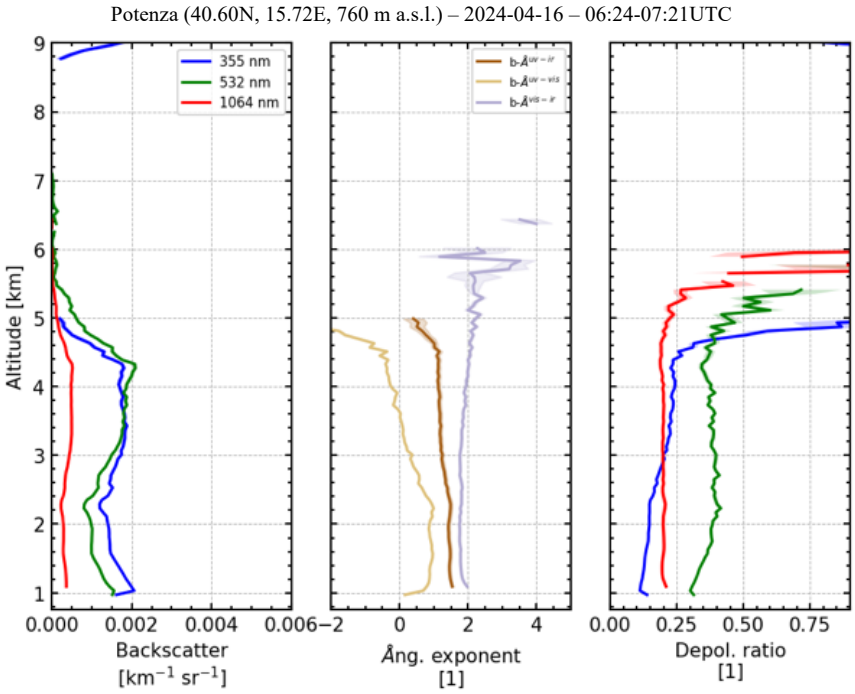

Figure 7: Case study 2: Optical characterization of the dust layer below 5-6 km observed on 16 April by CIAO lidar POLPO. From left to the right: aerosol backscatter at 355, 532, 1064nm, backscatter related Angström exponent, particle linear depolarization ratio

Finally, Figs. 5 and 8 indicate the presence of several clouds on the top of the dust layer presumably formed by heterogeneous nucleation due to dust particles. Moreover, right below the clouds there are regions where the concentration of the dust seems to temporarily decrease (see for example region below 3.5km asl at about 20:00UTC of 15 April). These regions with reduced aerosol concentration might be explained by scavenging processes induced by precipitations which evaporate before they arrive at ground. The above processes are particularly interesting for the study of aerosol-cloud interactions, which need further investigation beyond the scope of this report.

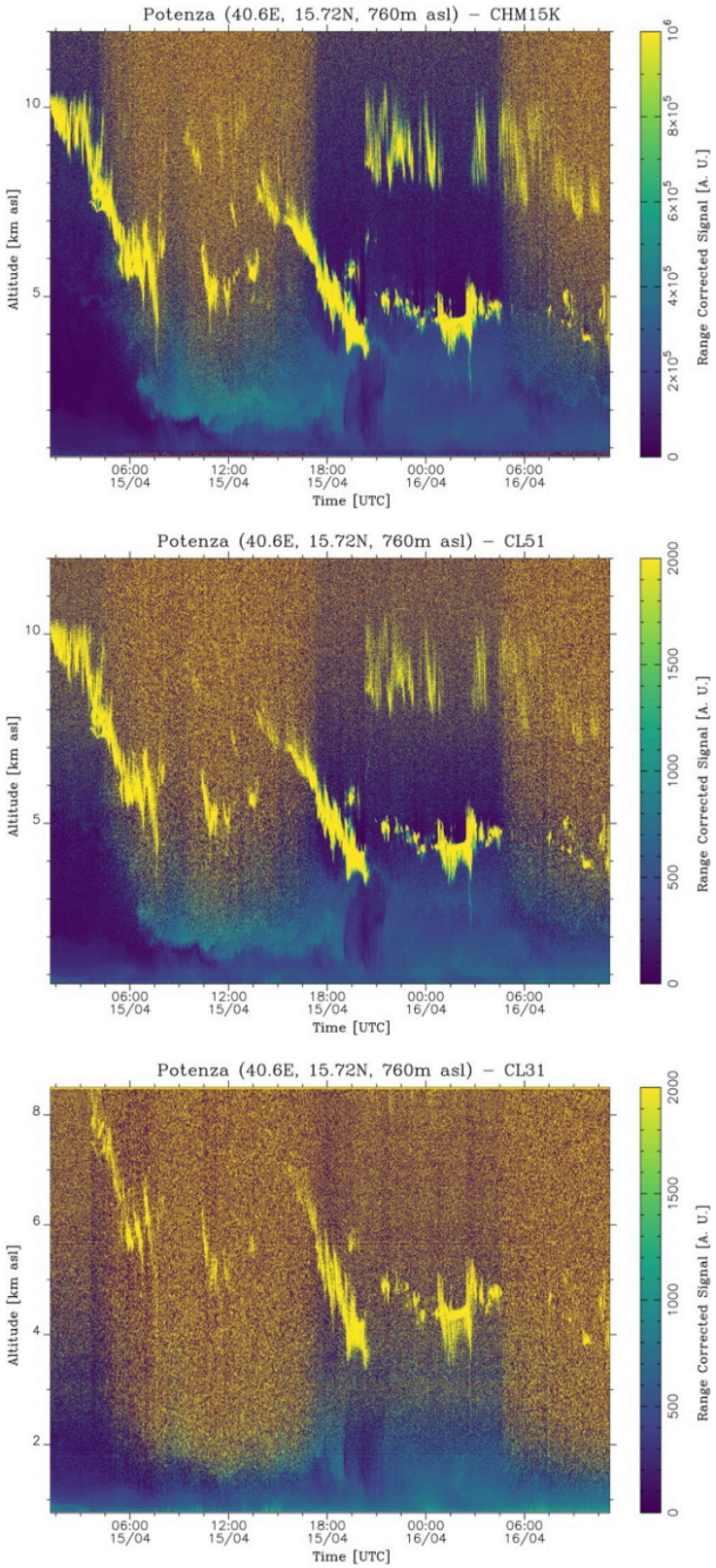

Figure 8: Case study 2: timeseries of range corrected signal measured by CHM15k (top), CL51 (middle) and CL31 (bottom) ceilometers.

4. MIPA DESCRIPTION

The composite image on which the proposed algorithm is applied consists in the temporal sequence of vertically resolved total attenuated backscatter lidar profiles. The proposed morphological image processing approach (MIPA) algorithm has no prior knowledge on ABLH and the image processing approach relies on:

- a block that reduces the vertical spatial resolution to reach a working spatial resolution, i.e. around 20 m, if the spatial resolution of the system is finer;
- a pre-processing step applied to the daily lidar data exploiting mathematical morphology;
- Canny's edge detection[4] applied to the pre-processed lidar data;
- a post-processing starting from the detected edges and based on both mathematical morphology and an object-based analysis to get the outcome.

The algorithm receives in input an image representing the timeseries of the total attenuated backscatter profiles measured by the lidar system. Thus, it is a matrix where the number of rows is related to the maximum height and the spatial resolution of the system, whereas, the number of columns is related to its temporal resolution and acquisition hours. A downsampling with a factor $\boldsymbol{R}$, which aims to reduce the bins' spatial resolution, is implemented by a low-pass filter along each column plus decimation with a factor $\boldsymbol{R}$. More specifically, a moving-average filter is simply applied as low-pass filtering. The support (i.e., the length of the sliding window) of the filter is $\boldsymbol{R}$, again. Thus, $\boldsymbol{R}$ is the unique tuning parameter that is selected to have a spatial resolution no finer than 20 m. This value has been set to avoid multiple edges corresponding to the same layer, thus having sharper and uniquely identifiable edges. Hence, $\boldsymbol{R}$ can be directly calculated from the system's spatial resolution by leading the initial product to the target spatial resolution. The outcome is an image used as input in the pre-processing step. This latter consists in applying a low-pass morphological filter based on half gradients[5] to obtain a new image. Such filter corresponds to the semi-sum of special operators called dilation and erosion[5]. This operator is used in the pre-processing phase assuming as structuring element a horizontal line (i.e., along the time direction) with length $\boldsymbol{l_{pre}}$. It enables us to smooth the lidar image along the horizontal axis (where the dynamics of the ABL is quite slow), directionally reducing the noise and preserving the vertical edges that will be of crucial importance for the next steps.

Afterwards, an edge detector is applied to the pre-processed image. We employed Canny's edge detector (the classical version available in commercial software as MATLAB) to get the first (rough) estimation of the edge map. The detected edges are indicated with 1; instead, the rest of the map (background) is labeled as 0. All the bins labeled as 1 are potential candidates to represent the ABLH.

Finally, the edge map is analyzed by using the following further signal processing:

- **Morphological filters post-processing**. This processing step is done to remove unrealistic edges (i.e., edges that vary too fast with respect to the dynamics of the ABL). Thus, we apply a series of directional low-pass morphological filters. In particular, the used filters are obtained by sequentially applying an opening and a closing operator[5] using as structuring

[4] Canny, J.: A computational approach to edge detection, IEEE Trans. Pattern Anal. Mach. Intel., PAMI-8, 679–698, 1986

[5] *Soille, P.*: **Morphological Image Analysis: Principles and Applications**, Springer-Verlag, Berlin, Heidelberg, 2003.

element a line with a length l_{post} and an angle θ with respect to horizontal direction. θ ranges from θ_{min} to θ_{max}.

- **Object-based post-processing**. As already mentioned, the detected edges are indicated with 1; instead, the rest of the map (background) is labeled as 0. We work on these edges extracting objects. The main concept is the use of the connectivity in an edge map, i.e., the ways in which the bins labeled as "*edge*" (which assume value 1 in the edge map) are spatially related to their neighbors. A bin declared as "*edge*" is said "*8-connected*" if there exists at least one bin belonging to its 8 neighborhoods, i.e. the adjacent bins in vertical, horizontal and diagonal directions, declared as "*edges*", as well. All the bins that are "*8-connected*" to each other form an object. Thus, several objects, clustering the bins declared as "*edges*", are collected and analyzed. An analysis about the spatial variability of these objects is performed. Indeed, if the absolute Euclidean distance between the mean of the heights for each extracted object (using the connectivity procedure explained above) and the related mean calculated on the objects in its neighborhood exceeds a threshold δ_{post}, this object is removed from the solution. Finally, the outcome, i.e., the estimated ABLH, is obtained by linearly interpolating the remaining objects in the edge map.

5. REFERENCE DATASET

We assume as reference the values of ABLH calculated from radiosounding data using an algorithm[6] based on both potential temperature and horizontal wind vertical profiles. It is important to underline that this algorithm delivers ABLH on the base of a thermodynamical definition of ABL. Basically the algorithm first identifies the ABL regime by examining the near-surface thermal gradient (difference in potential temperature) between two pre-selected close levels. Using specific threshold values, three different regimes can be determined: unstable regime (convective boundary layer), stable regime (stable boundary layer) and neutral regime (neutral residual layer).

Depending on the regime, different procedures are applied to get ABLH.

Table 1: Tab. 1: Radiosoundings performed in correspondence of the two considered case studies. The soundings are grouped by day. For each day, the launch time (hh:mm UTC) and the corresponding ABLH (m asl), calculated by applying to the radiosounding datasets the described algorithm[6], are reported. ABLHs are given in m asl (measurement site altitude is 760m) and the values in bold are the ones larger than 1060m asl (corresponding to the full overlap altitude of POLPO)

ABLH reference dataset								
2024-04-15	Time [UTC]		04:18	09:00	12:00	15:00	18:00	21:00
	ABLH [m asl]		849	**1480**	**1487**	1037	**1092**	892
2024-04-16	Time [UTC]	00:30	04:15	07:54				
	ABLH [m asl]	812	813	2296				
2024-04-28	Time [UTC]			08:00	13:00	15:30	18:00	21:00
	ABLH [m asl]			1634	2368	2351	1676	885

[6] *Shuyan Liu and Xin-Zhong Liang*, **Observed Diurnal Cycle Climatology of Planetary Boundary Layer Height, Journal of Climate**, Vol. 23, 2010, doi: 10.1175/2010JCLI3552.1

2024-04-29	Time[UTC]			08:10	11:00	16:00	19:00	22:00
	ABLH [m asl]			1537	2205	2232	1244	822
2024-04-30	Time[UTC]	00:45	04:00	08:00	10:59	14:07	17:03	20:00
	ABLH [m asl]	819	816	1039	2022	1904	2043	1065

For unstable or neutral regime, the ABLH is determined as the height at which an air parcel rising adiabatically from the ground becomes neutrally buoyant (again considering potential temperature variation). The level found in this way is considered a first guess and it is then corrected considering a threshold value of the first derivative of potential temperature.

For stable regime the ABLH is determined by applying specific thresholds on both first derivative of potential temperature and horizontal wind differences.

Further details about this algorithm can be found in the provided reference 6.

In Tab. 1, all the radiosoundings performed in correspondence of the two considered case studies are summarized. The soundings are grouped by day. For each day, the launch time (UTC) and the corresponding ABLH (m asl) calculated by applying the described algorithm are reported. Consequently, Tab. 1 provides the ABLH reference dataset we have used for MIPA *optimization/validation.* ABLH values in bold are the ones above the full overlap altitude of POLPO (300m agl).

6. MIPA VALIDATION

In this section, we discuss how MIPA has been validated and optimized considering the datasets corresponding to the two optimal case studies discussed in Sec. 3.1 and 3.2. It's worth noting that such case studies fulfill all the technical requisites for MIPA applicability discussed at the beginning of the Section 3 (in this sense they are optimal) but, at the same time, due to the strong dust intrusions characterizing both they represent a quite challenging dataset to evaluate the performance of MIPA to retrieve accurate ABLH in complex atmospheric scenario.

Fig. 9 shows the ABLH retrieved by MIPA (black curve) when applied to the 1064nm timeseries of total attenuated backscatter of the case study 1 (also reported in figure as color map). It's worth to note that the results shown have been obtained by MIPA using the optimized configuration parameters reported in Tab. 2. Gray dots in Fig. 9 provide the reference ABLH dataset given in Tab. 1 and calculated according to the methodology described in Sec. 5 using radiosounding data. MIPA performance will be evaluated on the basis of absolute differences with respect to the considered reference.

In general, during daytime conditions, ABLHs retrieved by MIPA are in good agreement with the reference ones. The expected temporal evolution of the ABL is well captured and the intrusions of the upper dust layers in the ABL do not seem to affect the outcomes, thus still obtaining reasonable ABLH estimates. More precisely, as expected, during the last day (30 April) the compression of the upper layer is responsible for a flatter evolution of ABLH with respect to the previous 2 days.

On the other hand, during nighttime conditions, ABLHs retrieved by MIPA overestimate the reference ones. To explain such behavior, it is important to highlight that MIPA retrieves the ABLH as the top of the first detected aerosol layer. This assumption is valid only if the ABL is above the

full overlap height of the lidar performing the measurements. During nighttime observations, this condition is typically not verified, and in this case the algorithm detects as the first edge the base of the layer close to the ABL top. Consequently, the overestimation occurring during nighttime is due to a limitation of the input dataset and not of the algorithm itself which ideally would have provided ABLH as accurate as in daytime conditions if the lidar measurements had covered regions closer to the ground.

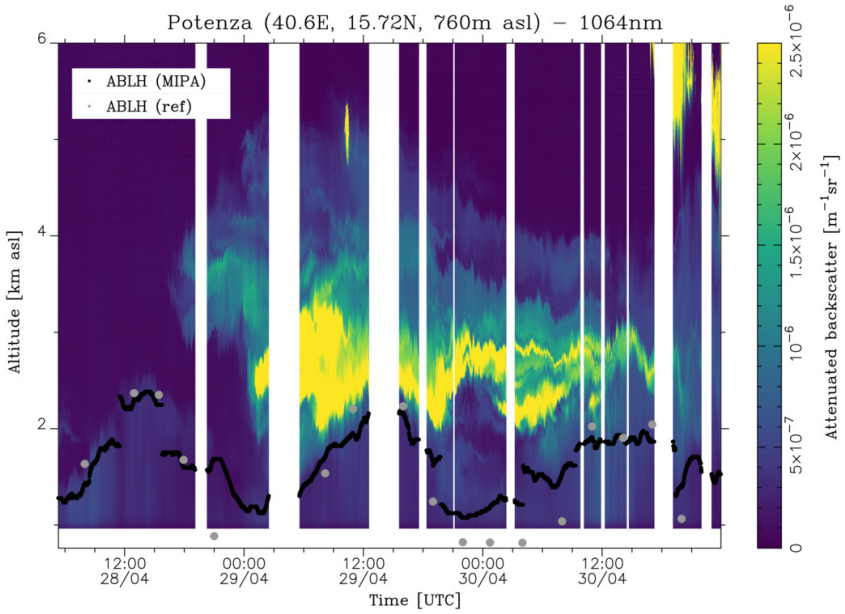

Figure 9: High-resolution timeseries of the total attenuated backscatter at 1064 nm measured for the first case study (28–30 April 2024). Time resolution is 60 s, vertical resolution is 3.75 m. The black curve shows the ABLH as retrieved by MIPA while the gray dots are the reference ABLH calculated from radiosondings.

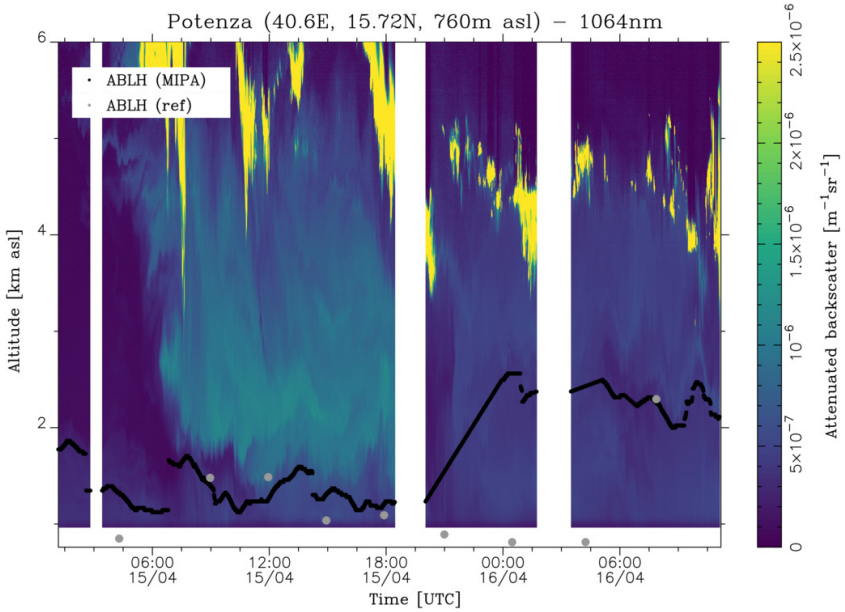

Figure 10: High-resolution timeseries of the total attenuated backscatter at 1064 nm measured for the second case study (15–16 April 2024). Time resolution is 60 s, vertical resolution is 3.75 m. The black curve shows the ABLH as retrieved by MIPA while the gray dots are the reference ABLH calculated from radiosondings.

MIPA results for the other case study are shown in Fig. 10. All the plotted quantities are the same already described for Fig. 9. As discussed in Sec. 3.2, right after 06:00 UTC on 15 April, an intense dust layer is clearly visible in the color map. This intense layer arrives over measurement site quite abruptly avoiding the ABL to evolve normally. This is confirmed by the very low values of ABLH retrieved by both MIPA and radiosoundings data between 09:00 and 18:00 UTC. After this period, the layer appears less intense and consequently the ABL can evolve to higher heights during the morning of the next day (16 April). Obviously, the mismatch between the retrieval and the reference from 15 April 19:00 up to 16 April 07:00 is due to the lack of lidar observations where the ABLH is located. As for the previous case study, in general, during daytime conditions, ABLHs retrieved by MIPA are in good agreement with the reference ones while during nighttime ABLHs retrieved by MIPA are overestimated for the same lidar overlap issue discussed earlier.

A statistical analysis of the absolute differences of ABLHs retrieved by MIPA with respect to the corresponding (in time) reference is given in Tab. 3 considering separately all reference points (all values in Tab. 1) and only reference points above the full overlap height of the lidar (bold values in Tab. 1). Tab. 3 shows the mean (Δ_{mean}), the median (Δ_{med}), the standard deviation (Δ_{SD}), the standard error (Δ_{SE}), the minimum (Δ_{min}) and the maximum (Δ_{max}) of the absolute differences between ABLH retrieved by MIPA and the corresponding reference points.

When all reference points are considered, a mean absolute difference of 365m is found ranging from a minimum value of 16m (corresponding to the radiosounding made on 30 April 14:07 UTC) to amaximum of 1750m (radiosounding made on 16 April 00:30 UTC). As already discussed earlier, during nighttime conditions, the input dataset we have used to validate MIPA is not suitable for the detection of ABLH values below the full overlap height of the lidar observations. Consequently, the statistical analysis including all the reference points contains bias due to:

1. inversion algorithm (MIPA)
2. instrumental limitations (ABLH values below lidar overlap height)
3. different ABL definitions (thermodynamic one in case of reference dataset, based on aerosol as ABL tracers in case of lidar dataset)

For a proper MIPA validation contributes coming from points 2 and 3 should be excluded from the statistical analysis as they both do not apply the specific algorithm used to retrieve ABLH (basically they are present whatever is the retrieval algorithm). To consider only differences due to MIPA we considered only the reference points above the considered lidar full overlap height (300m agl). In this way, differences due to the point 2 are obviously removed and differences due to the point 3 are minimized (the two mentioned ABL definitions are equivalent if the ABL is well-mixed, and this typically happens when the solar convective action is relevant, i.e. when the ABLH is not minimal). Accordingly, considering only these reference points, the mean absolute differences is reduced to 151m with a maximum of 373m (radiosounding performed on 29 April 19:00 UTC). These results prove that the optimized configuration of MIPA we have used can retrieve ABLH with a mean absolute difference with respect to the reference of 150m in all the cases in which the lidar observations allow to capture the ABLH.

It's important to note that all the MIPA retrievals reported in this document have been obtained using the same set of configuration parameters summarized in Tab. 2. Even if up to now the usage of MIPA has been considered only on HPL, this is a good indication of the robustness of MIPA. Further and deeper evaluations of this aspect of MIPA will be available when the algorithm will be applied on very different type of sensors like for example ceilometers. This is planned as next step to do. Note that in principle the only parameters that needs to be adapted to make MIPA working on different type of sensor is ***R***. Additionally, for the ceilometers the application of technique to increase the SNR could be necessary (prior to the application of MIPA) to get results with an accuracy similar to the one described in this deliverable.

Additionally, comparisons among MIPA and other traditional lidar ABLH retrieval techniques will also be carried out in the near future even if this topic has been already discussed in literature[7] showing in general better performance of MIPA with respect to the other approaches.

Table 2: Optimized MIPA configuration parameters used to produce all MIPA results described in this report (see Sec. 4 for the parameter description)

Parameter	*Description*	*Optimized value*
R	Input image down-sampling factor	6
l_{pre}	Length of pre-processing structuring element (horizontal line along the time direction)	3
l_{post}	Length of post-processing structuring element	4
θ_{min}	Minimum angle (with respect horizontal direction) of post-processing structuring element	-66°
θ_{max}	Maximum angle (with respect horizontal direction) of post-processing structuring element	66°
δ_{post}	Euclidean distance threshold among objects and related neighborhood objects	10

Table 3: Statistical analysis of the absolute differences with respect to the reference of the ABLH retrieved by MIPA on high-resolution timeseries of the total attenuated backscatter at 1064 nm for both the case studies considered. The mean (Δ_{mean}), the median (Δ_{med}), the standard deviation (Δ_{SD}), the standard error (Δ_{SE}), the minimum and the maximum of the absolute differences are given in meters. N is the number of points on which the statistics are carried out. The reference is assumed to be the ABLH calculated from the co-located radiosounding data.

	All reference points	*Only reference points above lidar full overlap height*
Δ_{mean} [m]	365	151
Δ_{med} [m]	240	116
Δ_{SD} [m]	434	105
Δ_{SE} [m]	85	26
Δ_{min} [m]	16	16
Δ_{max} [m]	1750	373
N	26	16

7. FUTURE DEVELOPMENT

As future developments we have planned to address the following items:

- evaluation of the optimized MIPA configuration over all the HPL measurement campaign datasets. We will check how MIPA works when it is applied to timeseries of total attenuated backscatter at shorter wavelengths.

[7] *Vivone, G., D'Amico, G., Summa, D., Lolli, S., Amodeo, A., Bortoli, D., and Pappalardo, G.*: **Atmospheric boundary layer height estimation from aerosol lidar: a new approach based on morphological image processing techniques**, Atmos. Chem. Phys., 21, 4249–4265, https://doi.org/10.5194/acp-21-4249-2021, 2021

- evaluation of the optimized MIPA configuration on ceilometer (LPL) measurement campaign datasets. This item is particularly important because it will give us the possibility to explore the limits of MIPA algorithm robustness. Ceilometer datasets have very different features with respect to HPL ones especially for what it concerns the reduced SNR. Moreover, the lower overlap of these sensors will provide more information about the MIPA ability to get reliable ABLHs closer to the ground.
- evaluation of ABLH retrieval using a multi-sensor approach.